ACS NANO

www.acsnano.org

ARTICLE

In Situ Spray Polymerization of Conductive Polymers for Personalized E-textiles

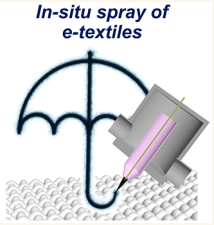
Taehoo Chang,[#] Semih Akin,[#] Seungse Cho,[#] Junsang Lee, Seul Ah Lee, Taewoong Park, Seokkyoon Hong, Tianhao Yu, Yuhyun Ji, Jonghun Yi, Sunland L. Gong, Dong Rip Kim, Young L. Kim, Martin Byung-Guk Jun,* and Chi Hwan Lee*

Cite This: https://doi.org/10.1021/acsnano.3c07283

Read Online

ACCESS | Metrics & More | Article Recommendations | Supporting Information

ABSTRACT: **E-textiles, also known as electronic textiles, seamlessly merge wearable technology with fabrics, offering comfort and unobtrusiveness and establishing a crucial role in health monitoring systems. In this field, the integration of custom sensor designs with conductive polymers into various fabric types, especially in large areas, has presented significant challenges. Here, we present an innovative additive patterning method that utilizes a dual-regime spray system, eliminating the need for masks and allowing for the programmable inscription of sensor arrays onto consumer textiles. Unlike traditional spray techniques, this approach enables in situ, on-the-fly polymerization of conductive polymers, enabling intricate designs with submillimeter resolution across fabric areas spanning several meters. Moreover, it addresses the nozzle clogging issues commonly encountered in such applications. The resulting e-textiles preserve essential fabric characteristics such as breathability, wearability, and washability while delivering exceptional sensing performance. A comprehensive investigation, combining experimental, computational, and theoretical approaches, was conducted to examine the critical factors influencing the operation of the dual-regime spraying system and its role in e-textile fabrication. These findings provide a flexible solution for producing e-textiles on consumer fabric items and hold significant implications for a diverse range of wearable sensing applications.**



KEYWORDS: *conductive polymers, e-textiles, wearable technology, additive patterning method, dual-regime spray system, sensor arrays, wearable sensing applications*

INTRODUCTION

E-textiles, a form of wearable technology that combines textiles with sensory capabilities, enable real-time and mobile monitoring of critical health signals, making them useful for various applications such as healthcare, military equipment, and wearable devices.[1−4] A range of traditional techniques for overcoating conductive materials, such as dip-coating, electrochemical deposition, chemical vapor deposition (CVD), physical vapor deposition (PVD), and direct printing, have been developed to produce e-textiles.[5−7] However, these techniques face challenges in creating intricate or personalized sensor designs for different fabric types due to the requirements of using heat, vacuum, precursors, plasma system, or vaporization process.[8,9] Additive patterning techniques, such as screen printing, inkjet printing, and three-dimensional (3D) dispensing, have been used to create custom sensor designs by employing either a shadow mask or direct writing.[10−14] However, these techniques may encounter challenges with clogging and high-throughput printing, particularly when covering large areas with active nanomaterials or molecules.[15,16]

A range of conductive materials, such as nanoparticles, nanowires, nanotubes, graphite, polymers, or composites, have been used to create e-textiles.[17−21] Among others, conductive polymers, such as polypyrrole (PPy), are of particular interest due to their desirable features for use in e-textiles, including mechanical softness, high electrical conductivity, ease of synthesis, compatibility with human skin, and stability against corrosion and oxidation.[22−24] However, achieving a uniform coating of conductive polymers onto different fabric types with high accuracy presents a challenge due to the nature of the wet polymerization process, which can lead to issues such as aggregation.[25] Reactive inkjet printing has emerged as a potent technique.[26−28] While this method enables in situ polymerization on substrates, it still faces constraints in scalable patterning due to the lack of efficient and rapid chemical mixing mechanisms. A recent advancement to address this issue is the in situ aerosol mixing using flow, which allows for compositional mixing of materials with high-throughput

Received: August 4, 2023
Revised: November 1, 2023
Accepted: November 2, 2023

Downloaded via PURDUE UNIV on November 11, 2023 at 12:58:18 (UTC).
See https://pubs.acs.org/sharingguidelines for options on how to legitimately share published articles.

© XXXX American Chemical Society

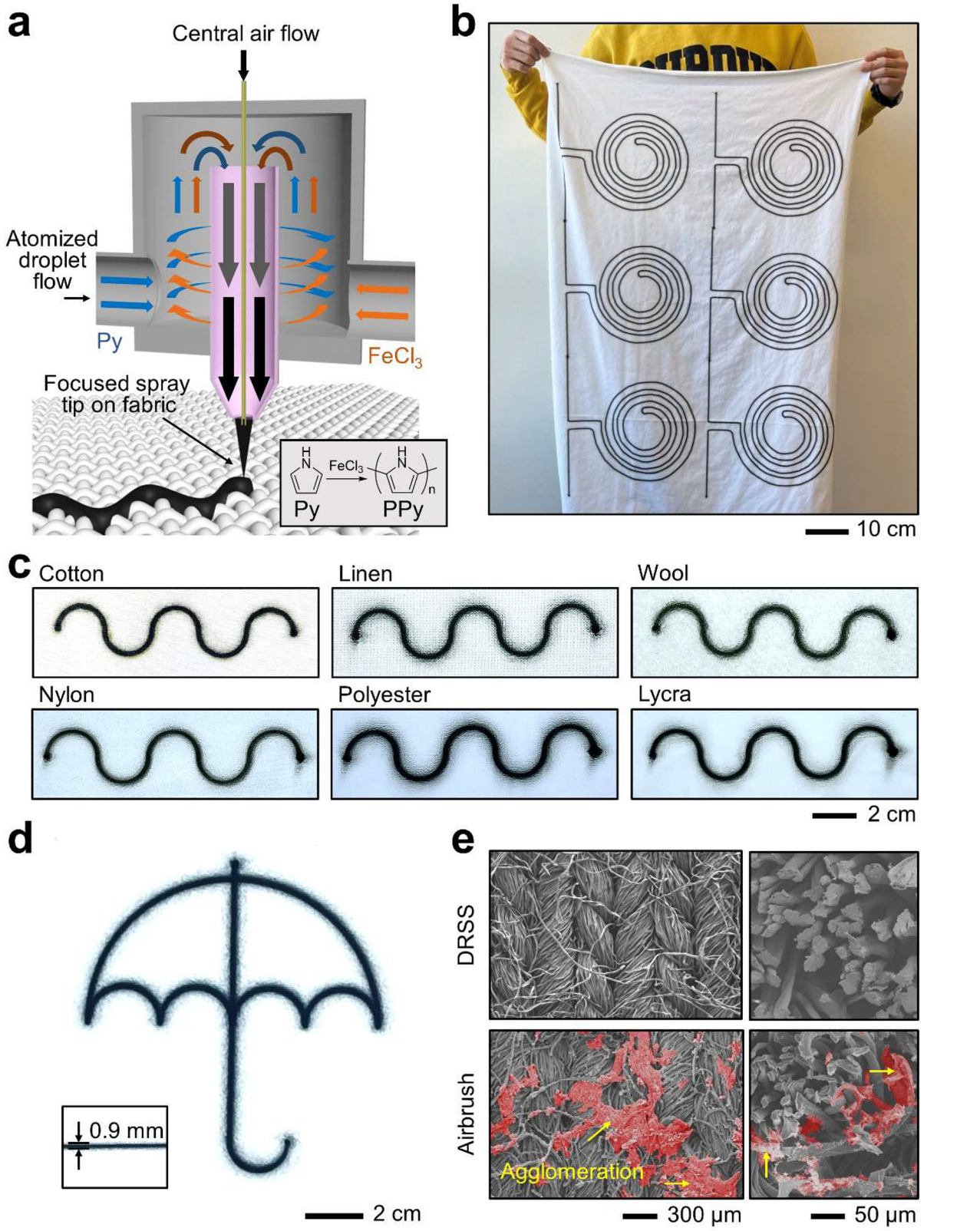


Figure 1. DRSS process. (a) Schematic illustration of the DRSS process to produce e-textiles. (b) Photograph of a large scale of PPy spray patterning onto white cotton fabric. (c) Photographs showing a serpentine pattern of PPy sprayed on different fabric types. (d) Photograph showing programmable umbrella-patterned PPy on cotton fabric with submillimeter resolution. (e) SEM images comparing the surface of PPy overcoated fabric produced by the DRSS and traditional airbrush.

printing.[29] Despite its great potential, in situ polymerization using flow presents challenges due to ongoing changes in viscosity during polymerization, which can disrupt flows. As a result, an advanced spray platform technology that facilitates high-throughput chemical mixing and high-speed spray printing simultaneously becomes essential.

https://doi.org/10.1021/acsnano.3c07283
ACS Nano XXXX, XXX, XXX−XXX

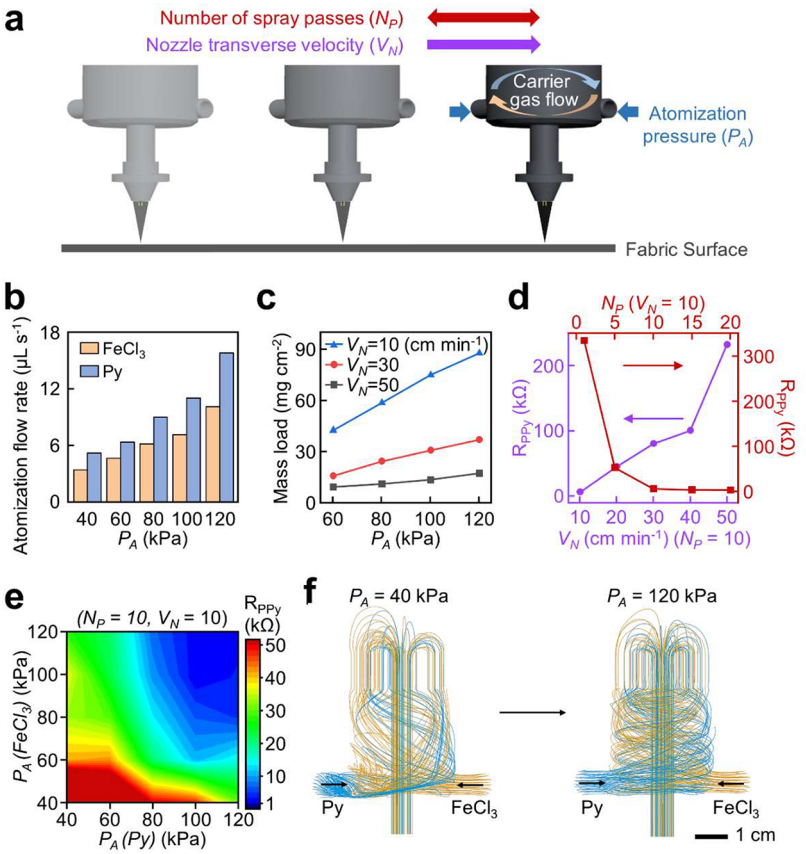


Figure 2. Optimal spray conditions. (a) Schematic illustration of the governing operational parameters in the DRSS process. (b) Atomization flow rate of Py and $FeCl_3$ over a range of P_A. (c) Mass load of PPy sprayed onto fabric as a function of P_A and V_N. (d) R_{PPy} as a function of N_P and V_N. (e) Color map of R_{PPy} as a function of P_A(Py) and P_A($FeCl_3$). (f) CFD results showing the streamlines of the carrier gas flow at P_A = 40 and 120 kPa, respectively.

Here, we present an additive patterning approach using a dual-regime spray system (DRSS), enabling precise, programmable, and mask-free inscription of sensor arrays onto consumer fabric items. The DRSS, unlike existing spraying techniques, provides advantages enabling in situ, on-the-fly polymerization of conductive polymers, such as PPy, while spraying intricate or personalized designs with submillimeter resolution over meter-scale areas on various fabric types. The use of DRSS minimizes the risk of nozzle clogging and polymer agglomeration, which are common issues resulting from overreaction of polymers in conventional dispensing techniques. Moreover, the kinetics of the spray polymerization can be readily controlled to tune the electrical conductivity of the conductive polymers. Proof-of-concept demonstrations include directly spraying conductive polymers into custom designs of stretchable strain gauges, with a gauge factor (GF) of over 85, onto various garments, such as masks, gloves, and stockinettes. These e-textiles are capable of continuously and unobtrusively tracking a range of human body movements from subtle (e.g., breathing) to large (e.g., joint bending) movements while minimally affecting the inherent fabric properties such as wearability, breathability, and washability.

RESULTS AND DISCUSSION

DRSS Process. Figure 1a schematically illustrates the DRSS process for in situ, on-the-fly spray polymerization of conductive polymers to produce e-textiles onto fabric items. The DRSS integrates two different air flow modules: (1) low-speed air flow that facilitates the atomization of chemicals and (2) high-speed focusing air flow that passes through the deposition nozzle mounted on a three-axis computer numerical control (CNC) gantry (Figure S1a).[30] The DRSS process began by atomizing fine droplets with two pneumatic atomizers made of glass (ArOmis, Inc., U.S.A.). One atomizer was filled with pyrrole (Py, monomer) dissolved in methanol, and the other was loaded with iron(III) chloride ($FeCl_3$, oxidizer) solution in a 1:7 ratio of water−methanol mixture by volume. Droplets of atomized chemicals were fed into a mixing chamber using low-speed airflow (<10 m s^{-1}) where PPy nanoparticles were synthesized by oxidative polymerization.[30] When Py and $FeCl_3$ met in the DRSS chamber, the polymerization process was initiated. This was further accelerated by the central airflow and finally completed upon spraying onto fabric surfaces. Figure S1b shows a serpentine line of PPy that was sprayed onto a white cotton fabric through the DRSS process. The black color indicates the complete polymerization of PPy, which was confirmed through UV−vis spectroscopy using a Cary-50 Varian instrument (Figure S1c). The highest speed of spraying PPy was about 50 cm min^{-1} (Video S1).

The DRSS offers several key advantages over the existing spraying techniques. First, the DRSS process was scalable over a meter scale with reasonable reproducibility (Figure 1b). Second, it requires no precursor coating, vacuum chamber, or heat treatment, making it compatible with a wide range of natural and synthetic fabric types (Figure 1c). Third, it can

https://doi.org/10.1021/acsnano.3c07283
ACS Nano XXXX, XXX, XXX−XXX

produce intricate designs, such as an umbrella shape, with submillimeter resolution without needing a shadow mask (Figure 1d). The resolution is determined by four key operational conditions: atomization pressure, nozzle transverse speed, central air velocity, and spray distance to fabric.[30] While using a shadow mask offers an alternative for achieving high resolution, it necessitates constant fabrication with each pattern change. The DRSS, through computer programmable patterning, ensures consistent coating quality on textiles by facilitating high mass loading and deep penetration coating through the fabric thickness. Moreover, it induces a minimal risk of contamination and clogging inside the DRSS chamber and nozzle after prolonged use (Figure S2a). This is due to its working principle that involves two atomizers which mix reactive chemicals within a chamber. The chemicals are swiftly propelled to the spray nozzle through air flow, ensuring that the chamber and nozzle remain uncontaminated. In contrast, when using a conventional airbrush (G22, Master Airbrush), irreparable contamination of the spray reservoir and clogging of the nozzle were observed after 90 min of use (Figure S2a). For a more detailed investigation, a nozzle was prepared using resin (Clear Resin, Formlabs) and utilized for an extended period of time (>90 min). It turned slightly blackish after 90 min of usage, but no signs of clogging were observed (Figure S2b). Lastly, it provides uniform and uninterrupted coating of PPy over the entire surface of fabric yarns, without agglomeration, in comparison to those using a conventional airbrush (Figure 1e). Additional scanning electron microscope (SEM) images, as presented in Figure S2c, not only corroborate consistent results but also substantiate the absence of any corrosion or alterations in the morphology of the fabric surface. The FT-IR analysis in Figure S2d, using the Thermo Nicolet Nexus 470 instrument, confirms that the PPy synthesized through DRSS has a similar quality to that of PPy synthesized through conventional dip-coating methods.[31,32] Furthermore, our approach for in situ spray polymerization is versatile and can be adaptable to other conductive polymers. For instance, polyaniline (PANI), known for its high conductivity, environmental stability, and biocompatibility, was successfully polymerized and directly written onto cotton fabric using DRSS (Figure S3a).[33] The synthesis was confirmed through FT-IR analysis (Figure S3b).

Optimal Spray Conditions. Identifying the optimal spray conditions for the DRSS process is crucial for successful in situ, on-the-fly polymerization of PPy. Figure 2a provides a schematic representation of the key operational parameters that govern the DRSS process including the number of spray passes (N_P), nozzle transverse velocity (V_N), atomization pressure (P_A), and carrier gas flow in the mixing chamber. Figure 2b shows the atomization flow rates of Py and $FeCl_3$ over a range of P_A values between 40 and 120 kPa. As P_A increased, the atomization flow rate also increased and reached its maximum value (approximately 16 μL s^{-1} for Py and 10 μL s^{-1} for $FeCl_3$) at P_A = 120 kPa. This indicates that a higher amount of reactive chemical agents was carried into the mixing chamber with increased P_A. The higher atomization flow rate observed in Py as compared to $FeCl_3$ can be primarily attributed to the substantially lower viscosity of Py (6.22×10^{-4} Pa s) relative to $FeCl_3$ (2.25×10^{-3} Pa s) (Figure S4a). The increased P_A led to a greater quantity of atomized Py and $FeCl_3$, as well as improved mixing inside the chamber. These factors led to accelerated polymerization and reduced resistance. Figure 2c presents the impact of P_A (60−120 kPa) and V_N (10−50 cm min^{-1}) on the mass loading of PPy sprayed onto a cotton fabric. The mass loading of PPy exhibited an increase with increasing P_A, reaching a maximum value of approximately 87 mg cm^{-1} at P_A = 120 kPa and V_N = 10 cm min^{-1}. At this point, the corresponding R_{PPy} was measured as 1.6 kΩ at N_P = 10 passes (Figure S4b). Conversely, when sprayed using a conventional airbrush, the resistance of PPy (R_{PPy}) remained considerably higher even at N_P = 20 passes due to widespread dispersion and a low mass load of PPy.

Figure 2d illustrates the effect of N_P and V_N on R_{PPy} over a range of N_P = 1−20 passes and V_N = 10−50 cm min^{-1}. The test specimen, which was sprayed in a straight line onto a cotton fabric, measured 3 × 50 mm^2 in size. The R_{PPy} tended to decrease as N_P increased or as V_N decreased. Figure 2e displays a color map of the resistance distribution across a range of P_A (40−120 kPa) for both Py and $FeCl_3$, demonstrating that the increased P_A resulted in a decrease in R_{PPy}. This color map also indicates that, by adjusting the P_A during the DRSS process, the R_{PPy} can be varied between 1.6−89.3 kΩ. To demonstrate this feature, four resistive heaters were sprayed onto a cotton fabric with the same width (6 mm) and serpentine shape but varying P_A = 90−120 kPa (Figure S5a). This resulted in a range of R_{PPy} from 0.8 to 3.3 kΩ, or a range of heat generation levels from 36 to 55 °C at an applied voltage of 30 V (Figure S5b). To further validate the reproducibility and uniformity of this method, a total of 10 identical serpentine patterns were crafted (Figure S6a). These patterns demonstrated consistent resistance (R_{PPy} = 5.05 ± 0.17 kΩ), highlighting minimal variations and emphasizing the method's dependable polymerization and patterning capabilities (Figure S6b).

Figure 2f displays the snapshot images of computational fluid dynamics (CFD) results, depicting the streamlines of the carrier gas flow at P_A = 40 and 120 kPa. The CFD domains and local grids of the mixing chamber and nozzle are shown in Figure S7a. As P_A increased, the carrier gas flow inside the mixing chamber became more uniform, resulting in improved mixing and polymerization of PPy. These CFD results were consistent with experimental data, indicating that PPy was fully polymerized at P_A = 120 kPa, resulting in a black color, whereas incomplete polymerization was observed as a yellow color at P_A = 40 kPa (Video S2). The P_A for both Py and $FeCl_3$ was balanced to prevent nonuniform carrier gas flow in the mixing chamber (Figure S7b). The concentration ratio of Py to $FeCl_3$ was maintained at 4:1 to provide the lowest R_{PPy} (54.3 ± 5.1 kΩ) (Figure S8a).[34] Methanol (MeOH) was used as a mixing solvent for both Py and $FeCl_3$, resulting in nearly 4-fold lower R_{PPy} compared to those obtained when using water (H_2O) and other polar solvents such as ethanol (EtOH) (Figure S8b). This can be attributed to the interaction between Py and MeOH, including their high miscibility, lower boiling point of Py, faster evaporation rate, and polarity, as well as the ability of MeOH to reduce the Coulomb interaction during polymerization.[35,36] Taken together, the optimal conditions to achieve highly uniform and conductive PPy were determined to be P_A = 120 kPa, N_P = 10 passes, and V_N = 10 cm min^{-1}, using a MeOH mixing solution with a Py/$FeCl_3$ concentration ratio of 4:1.

Benchtop Characterizations. For benchtop characterizations, test units of strain gauges were prepared by uniformly spraying PPy over the entire surface of a stretch cotton fabric (Tia Knight) in a size of 1 × 5 cm^2 using the optical DRSS

https://doi.org/10.1021/acsnano.3c07283
ACS Nano XXXX, XXX, XXX−XXX

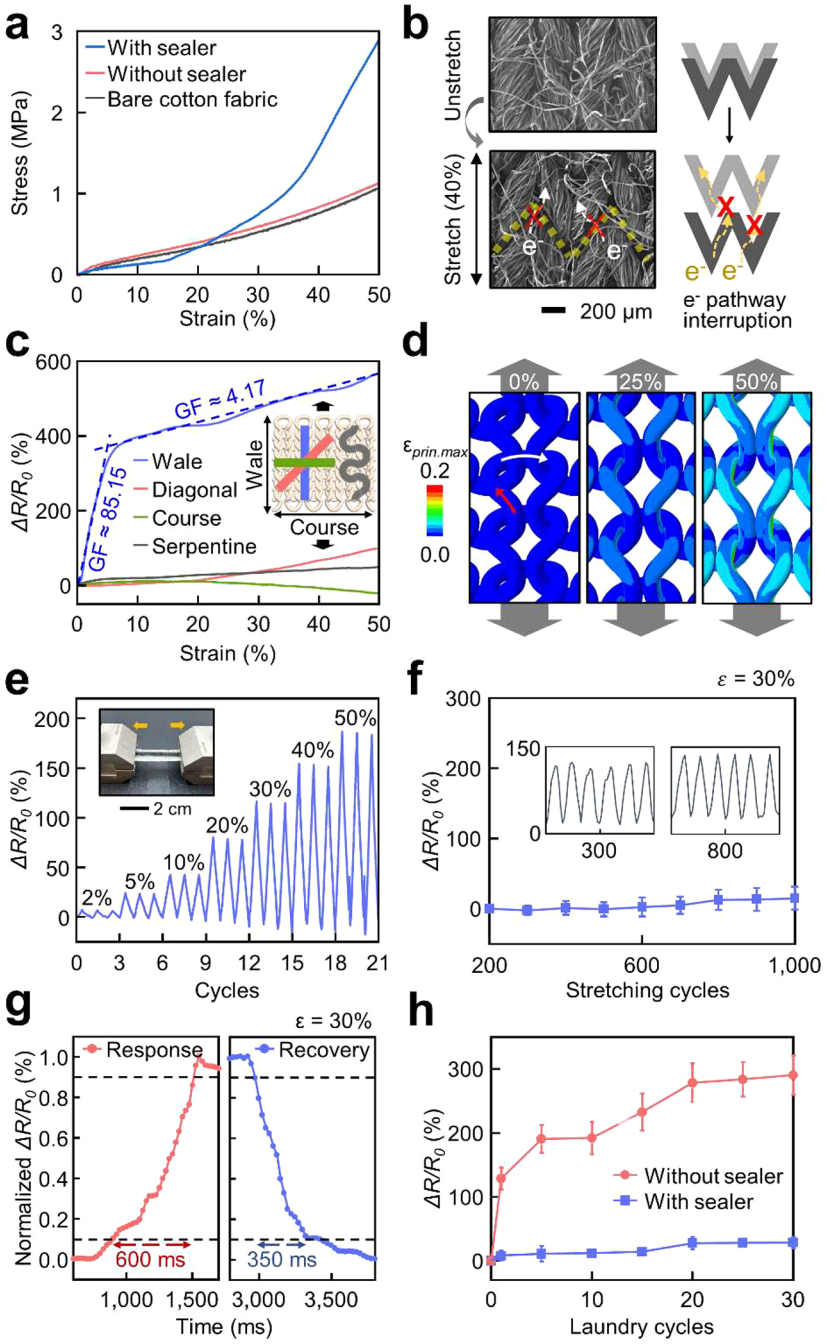


Figure 3. Benchtop characterizations. (a) Representative strain−stress curve of the test units with and without the presence of the sealer compared to a bare cotton fabric. (b) SEM image showing the test units without the sealer under stretching, along with a simplified schematic illustration of the strain response mechanism. (c) $\Delta R/R_0$ of the test units patterned in different shapes and directions under stretching up to 50% in the wale direction. (d) FEA results of the uniaxially stretched yarns. (e) $\Delta R/R_0$ of the test units under various strain loading conditions. (f) $\Delta R/R_0$ of the test units under 1,000 cycles of stretching at ε = 30%. (g) Strain response and recovery times of the test units. (h) $\Delta R/R_0$ of the test units under multiple laundry cycles with and without the presence of the sealer.

process. For improved durability, the test units were encapsulated with a silicone sealer (Ecoflex 00-30 diluted in Silicone Thinner; Smooth-On, Inc.) using a fine brush (Amazon). Figure 3a presents the mechanical strain−stress curves of the test units with (E = 3.8 MPa) and without (E = 2.2 MPa) the sealer, which are slightly higher or comparable to that of the bare cotton fabric (E = 2.1 MPa). Figure 3b provides an SEM image of a test unit without the sealer under stretching at the applied strain (ε) of 40% and a simplified illustration that shows how the stretching caused a disruption in the electrical pathways, resulting in an increase in R_{PPy}. As strain is applied, the knitted structure opens, leading to an increase in resistance. Figure S9a presents detailed serial SEM images taken during the application of strain to support this hypothesis. Figure 3c illustrates the variation in resistance ($\Delta R/R_0$) of the test units patterned differently in terms of direction and shape, including straight lines in the wale, diagonal, and course directions as well as serpentine lines in the wale direction. The test units were stretched in the wale direction up to 50%, which represents the maximum intrinsic

https://doi.org/10.1021/acsnano.3c07283
ACS Nano XXXX, XXX, XXX−XXX

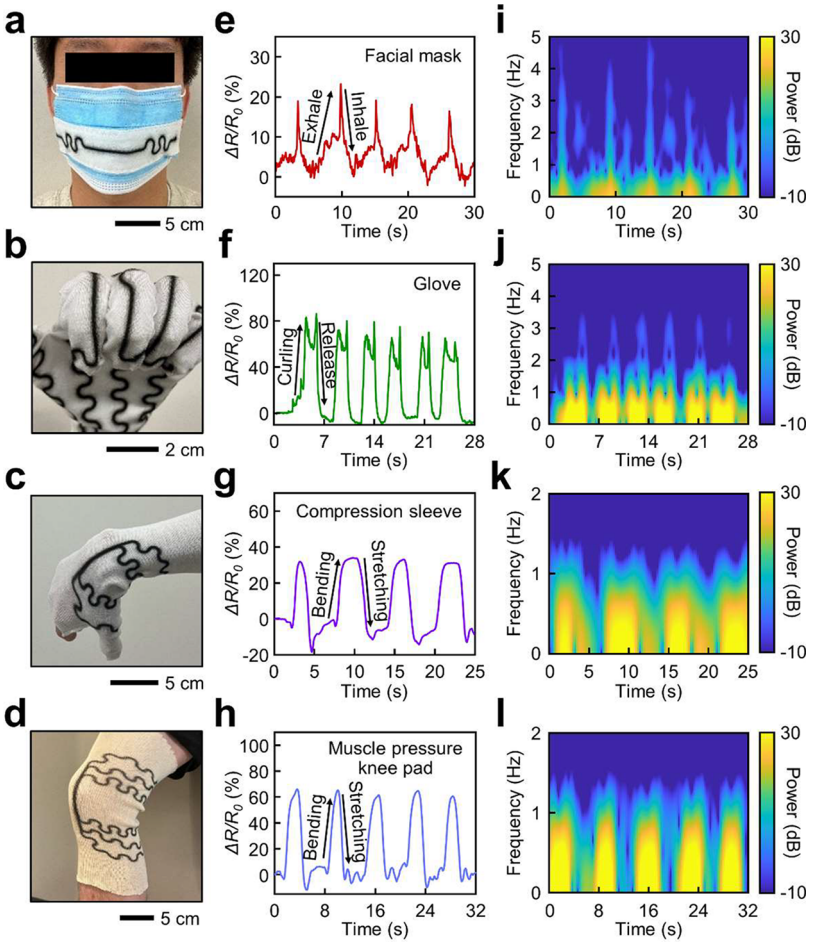


Figure 4. Proof-of-concept demonstration in wearable sensing applications. (a–d) Representative photographs of a test units in (a) a facial mask, (b) a cotton glove, (c) a compression sleeve, and (d) a muscle pressure knee pad. (e) Representative measurement data of respiration rate using the facial mask. (f) Representative measurement data of finger motion detection using the cotton glove. (g) Representative measurement data of wrist motion detection using the compression sleeve. (h) Representative measurement data of knee joint motion detection using the muscle pressure knee pad. (i–l) Time-series frequency spectral data set of (i) respiration rate, (j) finger motion detection, (k) wrist motion detection, and (l) knee joint movement.

stretch limit of the cotton fabric. The $\Delta R/R_0$ of the straight line in the wale direction exhibited a sharp increase at ε up to 5%, followed by a gradual increase at larger ε exceeding 50%, which resulted in gauge factors (GFs) of 85.15 and 4.17, respectively. Notably, our GF value is higher than that of strain gauges made of PPy in previous reports, as depicted in Figure S9b.[37−42] The traditional PPy-overcoated textile-based strain sensors are fabricated by dip-coating.[37−42] While the dip-coating method often results in overpolymerization and undesired aggregation, the DRSS approach provides seamless PPy overcoating on textile surface as depicted in Figure 1e and Figure S2c. We found clear empirical basis that this high-quality overcoating realized higher strain gauge factors since the seamless coating minimizes extra electronic connections between textile threads during stretching, as observed in Figure 3b. Meanwhile, the $\Delta R/R_0$ values for the straight lines in the diagonal and course directions showed weaker responses to strain, with a trend of wale > diagonal > course. Interestingly, a negative $\Delta R/R_0$ response was observed for the straight line in the course direction, attributed to the Poisson effect.[43] The $\Delta R/R_0$ response of the serpentine line was relatively imperceptible compared to that of the straight lines, likely due to its combination of orientations along the wale, diagonal, and course directions.[44,45]

Figure 3d presents the results of finite element analysis (FEA) that display the strain distribution across the uniaxially stretched yarns, which were coated with PPy to serve as electrical pathways, in the wale direction. The corresponding FEA results when the structure is stretched up to 50% strain are shown in Video S3. Due to the free sliding of the yarns, the yarns exhibited a smaller level of deformation than the applied strain. However, when the yarns were stretched in the wale direction, they extended freely without restriction, resulting in a larger deformation level (red arrow) than in other regions, except at the interfaces. The maximum strain was localized to a small region around the interfaces, where two yarns cross each other. In contrast, smaller strains were distributed along the course direction (white arrow) due to constraints imposed by entanglement. As the overall structure extended, the spaces between the yarns in the wale direction became more tightly packed, leading to additional contacts between the yarns and increased electrical pathways in the course direction. As a result, the $\Delta R/R_0$ of the test units increased dramatically when stretched in the wale direction due to the large concentration of strain caused by free extension, while minimal changes were

https://doi.org/10.1021/acsnano.3c07283
ACS Nano XXXX, XXX, XXX−XXX

observed when stretched in the course direction. When stretched in the diagonal direction, the test units displayed intermediate characteristics between those of the wale and course directions, resulting from the combined electrical pathways alternating both. These results suggest an effective design strategy for strain sensing, involving the placement of highly strain-responsive straight lines in the target location of the sensing area and the use of strain-insensitive serpentine lines as interconnectors (Figure S9c). These design strategies have often been utilized for various types of stretchable sensors.[46−50] The corresponding data for strain sensing, utilizing these designs across multiple stretching cycles ranging from 2% to 50% strain, are shown in Figure 3e. These results remained consistent over 1,000 cycles of stretching at ε = 30% (Figure 3f). To evaluate mechanical durability and reliability, additional deformations (folding and twisting at 360°) were conducted. In contrast to the strain response, negligible resistance changes were observed over 1,000 cycles of folding and twisting (Figure S10). The response and recovery times of the test units were measured as 600 and 350 ms at ε = 30%, respectively (Figure 3g). The recovery time was faster than the strain response time. This difference in response times can be attributed to the PPy-overcoated textiles resisting applied strain, with elastic recovery aiding during the recovery phase, as observed in previously reported PPy-overcoated textiles.[51,52]

Figure 3h presents that the $\Delta R/R_0$ of the test units was maintained over 30 cycles of washing with a standard laundry machine (ETW4100SQ0; Whirlpool). In the absence of the sealer, $\Delta R/R_0$ abruptly increased due to washout of PPy. Each laundry cycle consisted of three steps: (1) 10 min spinning in warm water at 30 °C with a fabric detergent (1 mg mL^{-1}, Jacquard synthrapol); (2) 5 min rinsing in cold water; and (3) 2 min spin-drying at room temperature. After being machine-washed, the test units were completely dried at ambient conditions (25 °C). Various drying temperatures, ranging from ambient to high (80 °C), were investigated to simulate different conditions, with the $\Delta R/R_0$ of the test units being exhibited as preserved, showing <1.3% variation (Figure S11a). The $\Delta R/R_0$ values of the test units remained unchanged even after immersion in a saline solution (Bausch + Lomb) for over 10 days. This solution, designed to mimic sweat, contained sodium (0.9 g L^{-1}) and potassium (0.2 g L^{-1}) at pH 7.0 (Figure S11b). In contrast, in the absence of the sealer, the $\Delta R/R_0$ increased and saturated at 150% after just 2 days of soaking due to the dedoping or migration of counterions, such as Cl^-, from the PPy into the saline.[53] Furthermore, the breathability of the test units, as indicated by the water vapor permeability, was maintained similar to that of the bare cotton fabric, given that the areal fill factor of the sealer was less than 40−50% (Figure S11c). These results suggest that adding a PPy overcoat with the sealer has minimal impact on the intrinsic fabric properties, while effectively protecting its electrical properties from environmental factors such as machine wash, detergent, and sweat.

Proof-of-Concept Demonstrations in Wearable Sensing Applications. Continuous and unobtrusive monitoring of strains, ranging from minor (<5%) to substantial (10−40%), in various body motions is of particular interest not only for understanding the mechanics of human movements, joint responses, and fatigue but also for aiding in the prevention and recovery of musculoskeletal injuries and disorders.[54,55] To showcase examples, several prototypes of strain gauges were prepared by spraying PPy across a range of consumer fabrics, including a facial mask (nonwoven 3-ply mask, Pure GEM), glove (white cotton gloves, Coohorn), compression sleeve (Wrist stockinette, Velpeau), and muscle pressure knee pad (Cotton stockinette roll, SoulGenie), for continuous monitoring of respiration rate, finger curl, wrist rotation, and knee flexion, respectively (Figure 4a−d). Complex designs of strain sensor arrays were effectively fabricated on various types of commercial garments using this method, and different body movements on the skin were successfully monitored by the sensors (Figure 4e−h). Real-time streams of these measurements are shown in Video S4. The ergonomic designs of the consumer fabrics ensured that the prototypes fit tightly to the different body parts and followed body motions accurately, resulting in high fidelity recordings of strains with large signal-to-noise ratios (>28.6 dB). To elaborate on human body movement through strain sensor measurement, time−frequency analysis and spectral data were implemented. The spectral data demonstrated that small body movements, such as respiration and small joint movement (finger), exhibited various frequency components (0−5 Hz) with low signal amplitudes (Figure 4i, j). In contrast, substantial body motions, like wrist and knee movement, were characterized by dominant low-frequency signal components (<1.5 Hz) with strong signal amplitude (Figure 4k, l). Importantly, no sign of skin irritation was observed during these demonstrations (Figure S12). Details of the skin irritation testing are described in the Methods section.

CONCLUSIONS

This research underscores the promising capacity of an innovative additive patterning method in transforming traditional clothing into personalized e-textiles while minimally affecting their intrinsic characteristics. We use a programmable DRSS to perform in situ, on-the-fly polymerization of conductive polymers, such as PPy, allowing direct spray writing of bespoke designs—from basic to complex patterns—for strain gauges. Our technique stands out for its high resolution (up to 0.9 mm line width), sensitivity (GF = 85.15), scalability (over 1 meter), and low electrical resistance (less than 1.6 kΩ). It also guarantees a seamless coating of conductive polymers and prevents nozzle blockage. The evenly distributed conductive polymers across the yarns allow the e-textiles to maintain their mechanical flexibility, breathability, and wearability. When used on stretchable clothing, these e-textiles ensure a comfortable fit, enabling precise strain monitoring across a wide spectrum from subtle to substantial body movements. Exploring beyond the foundational applications, e-textiles hold immense potential in consumer markets, such as interactive fashion, safety gear, and entertainment, offering opportunities for real-time environmental and biometric monitoring, dynamic user interaction, and immersive experiences. These emerging applications signify a convergence of technology and daily life, underscoring the need for continued exploration and innovation in this burgeoning field. Considering the inherent challenges and inefficiencies in chemical mixing associated with inkjet printing-based reactions, our DRSS method, which generates numerous micro-reactive droplets simultaneously, stands out as a compelling and predominant solution for achieving high-throughput chemical mixing and high-resolution spray printing. Ultimately, our approach enables the creation and development of personalized e-textiles, bringing together custom functionality and stylish designs.

https://doi.org/10.1021/acsnano.3c07283
ACS Nano XXXX, XXX, XXX−XXX

METHODS

In Situ, On-the-Fly Spray Polymerization of PPy. Two pneumatic glass atomizers (ArOmis Inc.) were used to prepare a solution of 2 M pyrrole (Py; Sigma-Aldrich) in methanol and a solution of 500 mM iron(III) chloride hexahydrate ($FeCl_3 \cdot 6H_2O$; Sigma-Aldrich) in a 1:7 (v/v) mixture of water and methanol. Oxygen plasma-treated stretchable cotton fabric (Etsy) was placed on a three-axis CNC gantry, with a 2 mm spray distance. Each atomization pressure was adjusted from 40 to 120 kPa. To mitigate the potential issue of the monomer (Py) reacting or changing its properties during atomization, it was crucial to utilize these glass atomizers and ensure that each atomization pressure was adjusted and maintained above 40 kPa, which facilitated optimal aerosol mixing and efficient polymerization. The spray nozzle automatically drew the programmed patterns, while a high-speed central air flow was maintained at a velocity of 100 m s^{-1} during spraying. The resulting black PPy-overcoated fabric was rinsed with water and dried at room temperature.

Evaluation of Atomization Power and Stable Droplet Formation. The atomization power was evaluated by calculating the Ohnesorge numbers (Oh) of Py and $FeCl_3$. The Oh number is expressed by the following equation:

$$Oh = \mu/\sqrt{\rho\sigma L} \tag{1}$$

where μ is for viscosity, ρ is for density, σ is for surface tension, and L is for droplet diameter, respectively. σ = 22.50 mN m^{-1} and L = 2 μm were assumed to be the same in both Py and $FeCl_3$. The densities of the Py and $FeCl_3$ solutions were measured as 0.8103 and 0.8954 g cm^{-3}, respectively. The Oh value is known to be inversely related to the driving atomization power. In this study, the Oh numbers of Py and $FeCl_3$ were calculated to be 0.103 and 0.355, respectively. Using the Oh numbers, the figure of merit ($Z = Oh^{-1}$, $2 < Z < 24$) for minimizing satellite droplets can be evaluated.[56] Our system fits within the appropriate Z range with $Z_{Py} \approx 9.7$ and $Z_{FeCl_3} \approx 2.8$ for satellite droplet formation.

Computational Fluid Dynamics Modeling. The flow domain of the DRSS was discretized using 4,138,825 hexahedral elements. Mass flow rate boundary conditions were applied to both the atomized droplet air flow (6.5×10^{-5} kg s^{-1}) and central air flow (2.2×10^{-5} kg s^{-1}). An adiabatic wall with a no-slip boundary condition was used on the entire side surface of the system. At the nozzle exit, the pressure outlet boundary condition was set to atmospheric pressure (1 bar). To model the cyclone effects in the mixing chamber, the standard k–ε turbulence model was used with turbulent intensity and viscosity ratio set at 5% and 10%, respectively. The governing equations for a steady compressible flow were solved by using Ansys-Fluent Version 19.1 software.

Continuity equation:

$$\nabla\cdot(\rho\vec{u})=0 \tag{2}$$

Momentum equation:

$$\nabla\cdot(\rho\vec{u}\vec{u})=-\nabla p+\nabla\cdot(\mu\nabla\vec{u}) \tag{3}$$

Turbulent kinetic energy (TKE) equation:

$$\frac{\partial(\rho k u_i)}{\partial x_i} = \frac{\partial}{\partial x_j}\left[\frac{\mu_t}{\sigma_k}\frac{\partial k}{\partial x_j}\right] + 2\mu_t E_{ij}E_{ij} - \rho\varepsilon \tag{4}$$

Rate of dissipation equation:

$$\frac{\partial(\rho\varepsilon v_i)}{\partial x_i} = \frac{\partial}{\partial x_j}\left[\frac{\mu_t}{\sigma_\varepsilon}\frac{\partial\varepsilon}{\partial x_j}\right] + 2C_{\varepsilon 1}\frac{\varepsilon}{k}\mu S_{ij}S_{ij} - C_{\varepsilon 2}\rho\frac{\varepsilon^2}{k} \tag{5}$$

$$\mu_t = \rho C_\mu \frac{k^2}{\varepsilon} \tag{6}$$

where, μ and ρ are the viscosity (Pa s) and density (kg m^{-3}) of air, respectively, ν (m s^{-1}) is the velocity, g is the gravitational constant, S_{ij} is the fluid strain rate sensor, and the turbulence model constants are $C_{\varepsilon 1}$ = 1.44, $C_{\varepsilon 2}$ = 1.92, C_μ = 0.09, and σ_ε = 1.3, respectively. The contours of the air velocity inside and outside of the nozzle with central air flow were obtained from numerical simulations.

Benchtop Characteristics. Chemical analysis was carried out using ultraviolet–visible spectroscopy (UV–vis; Cary-50) and Fourier-transform infrared spectroscopy (FT-IR; Thermo Nicolet Nexus 470). Microstructures were observed by using a field emission scanning electron microscope (FE-SEM; Hitachi). Mechanical testing was performed by using a motorized force measurement tester (ESM303, Mark-10; Willrich Precision Instruments), while electrical properties were simultaneously monitored by using a source measurement unit (Keithley 2400; Tektronix, Inc.).

Wearable Sensing Demonstrations in Human Subjects. The wearable sensing demonstrations involved two healthy adult males (aged 30–35 years) and were conducted in compliance with an Institutional Review Board (IRB) approval (protocol number: HYUIRB-202212-009-2). After volunteers wore our prototype e-textiles embedded with strain gauges, their motion was recorded in real time by using a custom-built LabView code (National Instruments) and a source measurement unit (Keithley 2400; Tektronix, Inc.). The data were captured at a sampling rate of 40 Hz.

Skin Irritation Testing. This method involves detecting the increasing concentration of hemoglobin on the surface of the skin when inflammation occurs, in order to quantify the inflammation caused by irritants.[57] Line-scan hyperspectral imaging technology was employed as demonstrated in previous research.[58] Hyperspectral images (hypercubes) of human skin were obtained using a monochrome camera (GS3-U3-120S6M-C; FLIR), with a slit width of 23 μm and a groove density of 150 mm^{-1}. An LED light source with a color temperature of 6,500 K (D65) was used for illumination, and spectral calibration of the spectrograph was performed using a xenon calibration light source that emitted multiple narrow peaks at specific wavelengths. The skin was imaged by using a fixed focal length lens (MVL25M1; Navitar) with a field of view as small as 10 × 10 mm^2. The same area was also imaged using a smartphone camera (iPhone 11 Pro; Apple) to capture RGB images. The samples, including bare cotton fabric and PPy-overcoated fabric with/without the sealer, were applied onto the medial antebrachial cutaneous of the forearm for approximately 1 h. 3 M tapes were attached to the same area for 1 h as a positive control. Hemoglobin content was compared before and after the experiment by acquiring images and performing a mechanical linear scan step at 0.25 mm. Data were acquired using a custom MATLAB interface, and a tissue reflectance spectral model was used to extract key hemodynamic parameters from the ground-truth hyperspectral image. To model light propagation in tissue, the theory of radiative transport and robust approximations, such as diffusion, Born, and empirical modeling, were used. The intensity reflected from a biological sample can be expressed as a function of λ in the visible range:

$$I_R(\lambda) = \left[b_1\left(\frac{\lambda}{\lambda_0}\right)^{b_2} + b_3\left(\frac{\lambda}{\lambda_0}\right)^{-4}\right] \times \exp[-b_4 \times \{b_5 \times \varepsilon_{HbO_2}(\lambda) + (1-b_5)\times\varepsilon_{Hb}(\lambda)\}] \tag{7}$$

where b_1, b_2, and b_3 are associated with the scattering (Mie or Rayleigh) contributions at λ_0 = 800 nm, $\varepsilon_{HbO_2}(\lambda)$ denotes the

https://doi.org/10.1021/acsnano.3c07283
ACS Nano XXXX, XXX, XXX–XXX

absorption coefficient of oxygenated hemoglobin (HbO_2), $\varepsilon_{Hb}(\lambda)$ denotes the absorption coefficient of deoxygenated hemoglobin (Hb), b_4 is the hemoglobin concentration multiplied by the optical path length, and b_5 is the blood oxygen saturation (sPO_2). In this study, the level of skin irritation was indicated by the hemoglobin contents multiplied by the optical path length (b_4), using eq 7. The fitting parameters were computed using the simplex search (Nelder–Mead) algorithm. The results of the calculated average hemoglobin contents on the skin clearly showed that there was no significant difference ($p < 0.05$) among bare cotton, PPy, and Ecoflex overcoat, while there was a significant difference ($p > 0.05$) with the result of the 3 M tape (Figure S12). This result suggests that PPy, with or without the sealer, caused no sign of skin irritation, demonstrating excellent biocompatibility with the skin.

Finite Element Analysis. The deformation behavior of the yarns was analyzed by finite element analysis (FEA) using the commercial software package Abaqus. A 7 × 7 array of unit yarn structures was designed with a yarn diameter of 180 μm, and periodic boundary conditions were applied to the outer surfaces of the unit structures at the edges of the array. A linear elastic model was utilized with an elastic modulus of 1 GPa and a Poisson's ratio of 0.3, and a self-contact model was employed with interaction properties of frictionless tangential behavior and hard contact normal behavior.

ASSOCIATED CONTENT

Supporting Information

The Supporting Information is available free of charge at https://pubs.acs.org/doi/10.1021/acsnano.3c07283.

Figures showing the schematic illustration and photograph of the DRSS, UV–vis results, photographs of clogged air brush and nonclogged DRSS nozzle, SEM images, FT-IR results, PANI synthesis results, results of viscosity and test units, heater applications, results of identical samples, CFD modeling details, R_{PPy} results prepared using different Py/$FeCl_3$ ratios and solvents, SEM images under various strain loading conditions, comparison with previous references, strain sensor design aspects, reliability results, results of dry different conditions, results of the sealant effect in saline solution, results of permeability, and results of skin irritation (PDF)

Video S1 showing real-time DRSS process (MP4)

Video S2 showing real-time in situ spray polymerization at P_A = 40 and 120 kPa (MP4)

Video S3 showing the FEA results showing the strain distributions across the yarns under applied strains up to 50% (MP4)

Video S4 showing real-time demonstration of the proof-of-concept in wearable sensing applications (MP4)

AUTHOR INFORMATION

Corresponding Authors

Martin Byung-Guk Jun − *School of Mechanical Engineering, Purdue University, West Lafayette, Indiana 47907, United States;* orcid.org/0000-0002-0512-7209; Email: mbgjun@purdue.edu

Chi Hwan Lee − *School of Materials Engineering, Purdue University, West Lafayette, Indiana 47907, United States; School of Mechanical Engineering and Weldon School of Biomedical Engineering, Purdue University, West Lafayette, Indiana 47907, United States;* orcid.org/0000-0002-4868-7054; Email: lee2270@purdue.edu

Authors

Taehoo Chang − *School of Materials Engineering, Purdue University, West Lafayette, Indiana 47907, United States*

Semih Akin − *School of Mechanical Engineering, Purdue University, West Lafayette, Indiana 47907, United States;* orcid.org/0000-0002-3644-7133

Seungse Cho − *Weldon School of Biomedical Engineering, Purdue University, West Lafayette, Indiana 47907, United States*

Junsang Lee − *Weldon School of Biomedical Engineering, Purdue University, West Lafayette, Indiana 47907, United States*

Seul Ah Lee − *Weldon School of Biomedical Engineering, Purdue University, West Lafayette, Indiana 47907, United States*

Taewoong Park − *Weldon School of Biomedical Engineering, Purdue University, West Lafayette, Indiana 47907, United States*

Seokkyoon Hong − *Weldon School of Biomedical Engineering, Purdue University, West Lafayette, Indiana 47907, United States;* orcid.org/0009-0007-6540-0389

Tianhao Yu − *School of Mechanical Engineering, Purdue University, West Lafayette, Indiana 47907, United States;* orcid.org/0000-0001-9637-352X

Yuhyun Ji − *Weldon School of Biomedical Engineering, Purdue University, West Lafayette, Indiana 47907, United States*

Jonghun Yi − *School of Mechanical Engineering, Hanyang University, Seoul 04763, South Korea*

Sunland L. Gong − *Weldon School of Biomedical Engineering, Purdue University, West Lafayette, Indiana 47907, United States; School of Medicine, Indiana University, Indianapolis, Indiana 46202, United States*

Dong Rip Kim − *School of Mechanical Engineering, Hanyang University, Seoul 04763, South Korea;* orcid.org/0000-0001-6398-9483

Young L. Kim − *Weldon School of Biomedical Engineering, Purdue University, West Lafayette, Indiana 47907, United States;* orcid.org/0000-0003-3796-9643

Complete contact information is available at: https://pubs.acs.org/10.1021/acsnano.3c07283

Author Contributions

#T.C., S.A., and S.C. contributed equally to this work. The manuscript was written through contributions of all authors. All authors have given approval to the final version of the manuscript.

Notes

The authors declare the following competing financial interest(s): A patent application related to the materials and process for in situ spray polymerization of conductive polymers has been submitted to the U.S. patent office for consideration and is currently pending.

ACKNOWLEDGMENTS

C.H.L. acknowledges funding supports from the Leslie A. Geddes Endowment at Purdue University. D.R.K. acknowledges the funding support from the Basic Science Research Program (NRF-2021R1A2C1011418) through the National Research Foundation of Korea (NRF) funded by the Ministry of Science and ICT of Korea.

https://doi.org/10.1021/acsnano.3c07283
ACS Nano XXXX, XXX, XXX−XXX

REFERENCES

(1) Yin, J.; Wang, S.; Di Carlo, A.; Chang, A.; Wan, X.; Xu, J.; Xiao, X.; Chen, J. Smart Textiles for Self-Powered Biomonitoring. *Med-X* **2023**, *1*, 3.

(2) Chen, G.; Xiao, X.; Zhao, X.; Tat, T.; Bick, M.; Chen, J. Electronic Textiles for Wearable Point-of-Care Systems. *Chem. Rev.* **2022**, *122* (3), 3259−3291.

(3) Wang, H.; Zhang, Y.; Liang, X.; Zhang, Y. Smart Fibers and Textiles for Personal Health Management. *ACS Nano* **2021**, *15* (8), 12497−12508.

(4) Huang, L.; Lin, S.; Xu, Z.; Zhou, H.; Duan, J.; Hu, B.; Zhou, J. Fiber-based Energy Conversion Devices for Human-Body Energy Harvesting. *Adv. Mater.* **2020**, *32*, 1902034.

(5) Vaghasiya, J. V.; Mayorga-Martinez, C. C.; Vyskočil, J.; Pumera, M. Black Phosphorous-Based Human-Machine Communication Interface. *Nat. Commun.* **2023**, *14*, 2.

(6) Libanori, A.; Chen, G.; Zhao, X.; Zhou, Y.; Chen, J. Smart Textiles for Personalized Healthcare. *Nat. Electron.* **2022**, *5*, 142−156.

(7) Xiong, J.; Chen, J.; Lee, P. S. Functional Fibers and Fabrics for Soft Robotics, Wearables, and Human−Robot Interface. *Adv. Mater.* **2021**, *33*, 2002640.

(8) Meng, K.; Xiao, X.; Wei, W.; Chen, G.; Nashalian, A.; Shen, S.; Xiao, X.; Chen, J. Wearable Pressure Sensors for Pulse Wave Monitoring. *Adv. Mater.* **2022**, *34*, 2109357.

(9) Pyo, S.; Lee, J.; Bae, K.; Sim, S.; Kim, J. Recent Progress in Flexible Tactile Sensors for Human-Interactive Systems: from Sensors to Advanced Applications. *Adv. Mater.* **2021**, *33*, 2005902.

(10) Yin, L.; Cao, M.; Kim, K. N.; Lin, M.; Moon, J. M.; Sempionatto, J. R.; Yu, J.; Liu, R.; Wicker, C.; Trifonov, A.; Zhang, F.; Hu, H.; Moreto, J. R.; Go, J.; Xu, S.; Wang, J. A Stretchable Epidermal Sweat Sensing Platform with an Integrated Printed Battery and Electrochromic Display. *Nat. Electron.* **2022**, *5*, 694−705.

(11) Zub, K.; Hoeppener, S.; Schubert, U. S. Inkjet Printing and 3D Printing Strategies for Biosensing, Analytical, and Diagnostic Applications. *Adv. Mater.* **2022**, *34*, 2105015.

(12) Dong, C.; Leber, A.; Yan, D.; Banerjee, H.; Laperrousaz, S.; Das Gupta, T.; Shadman, S.; Reis, P. M.; Sorin, F. 3D Stretchable and Self-Encapsulated Multimaterial Triboelectric Fibers. *Sci. Adv.* **2022**, *8*, No. eabo0869.

(13) Zhao, X.; Zhou, Y.; Xu, J.; Chen, G.; Fang, Y.; Tat, T.; Xiao, X.; Song, Y.; Li, S.; Chen, J. Soft Fibers with Magnetoelasticity for Wearable Electronics. *Nat. Commun.* **2021**, *12*, 6755.

(14) Lv, J.; Thangavel, G.; Li, Y.; Xiong, J.; Gao, D.; Ciou, J.; Tan, M. W.; Aziz, I.; Chen, S.; Chen, J.; Zhou, X.; Poh, W. C.; Lee, P. S. Printable Elastomeric Electrodes with Sweat-Enhanced Conductivity for Wearables. *Sci. Adv.* **2021**, *7*, No. eabg8433.

(15) Zub, K.; Hoeppener, S.; Schubert, U. S. Inkjet Printing and 3D Printing Strategies for Biosensing, Analytical, and Diagnostic Applications. *Adv. Mater.* **2022**, *34*, 2105015.

(16) Du, X.; Wankhede, S. P.; Prasad, S.; Shehri, A.; Morse, J.; Lakal, N. A Review of Inkjet Printing Technology for Personalized-Healthcare Wearable Devices. *J. Mater. Chem. C* **2022**, *10*, 14091−14115.

(17) Islam, M. R.; Afroj, S.; Novoselov, K. S.; Karim, N. Smart Electronic Textile-Based Wearable Supercapacitors. *Adv. Sci.* **2022**, *9*, 2203856.

(18) Zhou, T.; Yu, Y.; He, B.; Wang, Z.; Xiong, T.; Wang, Z.; Liu, Y.; Xin, J.; Qi, M.; Zhang, H.; Zhou, X.; Gao, L.; Cheng, Q.; Wei, L. Ultra-Compact MXene Fibers by Continuous and Controllable Synergy of Interfacial Interactions and Thermal Drawing-Induced Stresses. *Nat. Commun.* **2022**, *13*, 4564.

(19) Nie, M.; Li, B.; Hsieh, Y. L.; Fu, K. K.; Zhou, J. Stretchable One-Dimensional Conductors for Wearable Applications. *ACS Nano* **2022**, *16* (12), 19810−19839.

(20) Na, Y. W.; Cheon, J. Y.; Kim, J. H.; Jung, Y.; Lee, K.; Park, J. S.; Park, J. Y.; Song, K. S.; Lee, S. B.; Kim, T.; Yang, S. J. All-in-One Flexible Supercapacitor with Ultrastable Performance under Extreme Load. *Sci. Adv.* **2022**, *8*, No. eabl8631.

(21) Zheng, L.; Zhu, M.; Wu, B.; Li, Z.; Sun, S.; Wu, P. Conductance-Stable Liquid Metal Sheath-Core Microfibers for Stretchy Smart Fabrics and Self-Powered Sensing. *Sci. Adv.* **2021**, *7*, No. eabg4041.

(22) Liman, M. L. R.; Islam, M. T.; Hossain, M. M. Mapping the Progress in Flexible Electrodes for Wearable Electronic Textiles: Materials, Durability, and Applications. *Adv. Electron. Mater.* **2022**, *8*, 2100578.

(23) Peng, S.; Yu, Y.; Wu, S.; Wang, C. H. Conductive Polymer Nanocomposites for Stretchable Electronics: Material Selection, Design, and Applications. *ACS Appl. Mater. Interfaces* **2021**, *13*, 43831−43854.

(24) Pang, A. L.; Arsad, A.; Ahmadipour, M. Synthesis and Factor Affecting on the Conductivity of Polypyrrole: a Short Review. *Polym. Adv. Technol.* **2021**, *32*, 1428−1454.

(25) Zea, M.; Texidó, R.; Villa, R.; Borrós, S.; Gabriel, G. Specially Designed Polyaniline/Polypyrrole Ink for a Fully Printed Highly Sensitive pH Microsensor. *ACS Appl. Mater. Interfaces* **2021**, *13* (28), 33524−33535.

(26) Teo, M. Y.; Stuart, L.; Devaraj, H.; Liu, C. Y.; Aw, K. C.; Stringer, J. The *in situ* Synthesis of Conductive Polyaniline Patterns Using Micro-Reactive Inkjet Printing. *J. Mater. Chem. C* **2019**, *7*, 2219−2224.

(27) Stempien, Z.; Rybicki, T.; Rybicki, E.; Kozanecki, M.; Szynkowska, M. I. *In-situ* Deposition of Polyaniline and Polypyrrole Electroconductive Layers on Textile Surfaces by the Reactive Ink-Jet Printing Technique. *Synth. Met.* **2015**, *202*, 49−62.

(28) Smith, P. J.; Morrin, A. Reactive Inkjet Printing. *J. Mater. Chem.* **2012**, *22*, 10965−10970.

(29) Zeng, M.; Du, Y.; Jiang, Q.; Kempf, N.; Wei, C.; Bimrose, M. V.; Tanvir, A. N. M.; Xu, H.; Chen, J.; Kirsch, D. J.; Martin, J.; Wyatt, B. C.; Hayashi, T.; Saeidi-Javash, M.; Sakaue, H.; Anasori, B.; Jin, L.; McMurtrey, M. D.; Zhang, Y. High-Throughput Printing of Combinatorial Materials from Aerosols. *Nature* **2023**, *617*, 292−298.

(30) Chang, T.; Akin, S.; Kim, M. K.; Murray, L.; Kim, B.; Cho, S.; Huh, S.; Teke, S.; Couetil, L.; Jun, M. B. G.; Lee, C. H. A Programmable Dual-Regime Spray for Large-Scale and Custom-Designed Electronic Textiles. *Adv. Mater.* **2022**, *34*, 2108021.

(31) Wang, F.; Li, Q.; Park, J. O.; Zheng, S.; Choi, E. Ultralow Voltage High-Performance Bioartificial Muscles Based on Ionically Crosslinked Polypyrrole-Coated Functional Carboxylated Bacterial Cellulose for Soft Robots. *Adv. Funct. Mater.* **2021**, *31*, 2007749.

(32) Huang, J.; Li, J.; Xu, X.; Hua, L.; Lu, Z. *In Situ* Loading of Polypyrrole onto Aramid Nanofiber and Carbon Nanotube Aerogel Fibers as Physiology and Motion Sensors. *ACS Nano* **2022**, *16* (5), 8161−8171.

(33) Zhang, T.; Zhang, S.; Li, L.; Hu, Y.; Liu, X.; Lee, J. Y. Self-Decoupled Oxygen Electrocatalysis for Ultrastable Rechargeable Zn-Air Batteries with Mild-Acidic Electrolyte. *ACS Nano* **2023**, *17* (17), 17476−17488.

(34) Deng, J.; Wang, X.; Guo, J.; Liu, P. Effect of the Oxidant/Monomer Ratio and the Washing Post-Treatment on Electrochemical Properties of Conductive Polymers. *Ind. Eng. Chem. Res.* **2014**, *53* (35), 13680−13689.

(35) Wyatt, Q. K.; Vaninger, M.; Paranamana, N. C.; Heitmann, T. W.; Kaiser, H.; Young, M. J. Oxidative Molecular Layer Deposition of Amine-Containing Conjugated Polymer Thin Films. *ACS Appl. Polym. Mater.* **2022**, *4* (8), 6156−6168.

(36) Lee, J. E.; Lee, Y.; Ahn, K. J.; Huh, J.; Shim, H. W.; Sampath, G.; Im, W. B.; Huh, Y. I.; Yoon, H. Role of Co-Vapors in Vapor Deposition Polymerization. *Sci. Rep.* **2015**, *5*, 8420.

(37) Yang, K.; Cheng, H.; Wang, B.; Tan, Y.; Ye, T.; Yang, Y.; Wang, C. Highly Durable and Stretchable $Ti_3C_2T_x$/PPy-Fabric-Based Strain Sensor for Human-Motion Detection. *Adv. Mater. Technol.* **2022**, *7*, 2100675.

(38) Wang, B.; Yang, K.; Cheng, H.; Ye, T.; Wang, C. A Hydrophobic Conductive Strip with Outstanding One-Dimensional Stretchability for Wearable Heater and Strain Sensor. *Chem. Eng. J.* **2021**, *404*, 126393.

https://doi.org/10.1021/acsnano.3c07283
ACS Nano XXXX, XXX, XXX−XXX

(39) Shen, H.; Ke, H.; Feng, J.; Jiang, C.; Wei, Q.; Wang, Q. Highly Sensitive and Stretchable c-MWCNTs/PPy Embedded Multidirectional Strain Sensor Based on Double Elastic Fabric for Human Motion Detection. *Nanomaterials* **2021**, *11*, 2333.
(40) Chen, X.; Li, B.; Qiao, Y.; Lu, Z. Preparing Polypyrrole-Coated Stretchable Textile via Low-Temperature Interfacial Polymerization for Highly Sensitive Strain Sensor. *Micromachines* **2019**, *10* (11), 788.
(41) Hao, D.; Xu, B.; Cai, Z. Polypyrrole Coated Knitted Fabric for Robust Wearable Sensor and Heater. *J. Mater. Sci. Mater. El.* **2018**, *29*, 9218−9226.
(42) Hu, J.; Zhou, S.; Shi, J.; Zhang, H.; Zhu, F.; Yang, X. Determinants of Electrical Resistance Change of *in situ* PPy-Polymerized Stretch Plain Woven Fabric under Uniaxial Tensile Strain. *J. Text. Inst.* **2017**, *108*, 1545−1551.
(43) Yang, Q.; Liu, N.; Yin, J.; Tian, H.; Yang, Y.; Ren, T. L. Understanding the Origin of Tensile Response in a Graphene Textile Strain Sensor with Negative Differential Resistance. *ACS Nano* **2022**, *16* (9), 14230−14238.
(44) La, T. G.; Qiu, S.; Scott, D. K.; Bakhtiari, R.; Kuziek, J. W. P.; Mathewson, K. E.; Rieger, J.; Chung, H. J. Two-layered and stretchable e-textile patches for wearable healthcare electronics. *Adv. Healthcare Mater.* **2018**, *7*, 1801033.
(45) Yoon, J.; Jeong, Y.; Kim, H.; Yoo, S.; Jung, H. S.; Kim, Y.; Hwang, Y.; Hyun, Y.; Hong, W. K.; Lee, B. H.; Choa, S. H.; Ko, H. C. Robust and stretchable indium gallium zinc oxide-based electronic textiles formed by cilia-assisted transfer printing. *Nat. Commun.* **2016**, *7*, 11477.
(46) Ouyang, W.; Lu, W.; Zhang, Y.; Liu, Y.; Kim, J. U.; Shen, H.; Wu, Y.; Luan, H.; Kilner, K.; Lee, S. P.; Lu, Y.; Yang, Y.; Wang, J.; Yu, Y.; Wegener, A. J.; Moreno, J. A.; Xie, Z.; Wu, Y.; Won, S. M.; Kwon, K.; Wu, C.; Bai, W.; Guo, H.; Liu, T. L.; Bai, H.; Monti, G.; Zhu, J.; Madhvapathy, S. R.; Trueb, J.; Stanslaski, M.; Higbee-Dempsey, E. M.; Stepien, I.; Ghoreishi-Haack, N.; Haney, C. R.; Kim, T. I.; Huang, Y.; Ghaffari, R.; Banks, A. R.; Jhou, T. C.; Good, C. H.; Rogers, J. A. A wireless and battery-less implant for multimodal closed-loop neuromodulation in small animals. *Nat. Biomed. Eng.* **2023**, *7*, 1252−1269.
(47) Song, J. W.; Ryu, H.; Bai, W.; Xie, Z.; Vázquez-Guardado, A.; Nandoliya, K.; Avila, R.; Lee, G.; Song, Z.; Kim, J.; Lee, M. K.; Liu, Y.; Kim, M.; Wang, H.; Wu, Y.; Yoon, H. J.; Kwak, S. S.; Shin, J.; Kwon, K.; Lu, W.; Chen, X.; Huang, Y.; Ameer, G. A.; Rogers, J. A. Bioresorbable, wireless, and battery-free system for electrotherapy and impedance sensing at wound sites. *Sci. Adv.* **2023**, *9*, No. eade4687.
(48) Yan, Z.; Xu, D.; Lin, Z.; Wang, P.; Cao, B.; Ren, H.; Song, F.; Wan, C.; Wang, L.; Zhou, J.; Zhao, X.; Chen, J.; Huang, Y.; Duan, X. Highly stretchable van der Waals thin films for adaptable and breathable electronic membranes. *Science* **2022**, *375*, 852−859.
(49) Kim, J. H.; Marcus, C.; Ono, R.; Sadat, D.; Mirzazadeh, A.; Jens, M.; Fernandez, S.; Zheng, S.; Durak, T.; Dagdeviren, C. A conformable sensory face mask for decoding biological and environmental signals. *Nat. Electron.* **2022**, *5*, 794−807.
(50) Yin, L.; Kim, K. N.; Lv, J.; Tehrani, F.; Lin, M.; Lin, Z.; Moon, J. M.; Ma, J.; Yu, J.; Xu, S.; Wang, J. A self-sustainable wearable multimodular E-textile bioenergy microgrid system. *Nat. Commun.* **2021**, *12*, 1542.
(51) Wang, B.; Peng, J.; Yang, K.; Cheng, H.; Yin, Y.; Wang, C. Multifunctional Textile Electronic with Sensing, Energy Storing, and Electrothermal Heating Capabilities. *ACS Appl. Mater. Interfaces* **2022**, *14*, 22497−22509.
(52) Zhou, Y.; Liao, H.; Qi, Q.; Guo, C.; Qi, K.; Ou, K.; He, J.; Wang, H.; Wang, R.; Chen, X. Polypyrrole-Coated Graphene Oxide-Doped Polyacrylonitrile Nanofibers for Stretchable Strain Sensors. *ACS Appl. Nano Mater.* **2022**, *5*, 8224−8231.
(53) Tang, W.; Yin, L.; Sempionatto, J. R.; Moon, J. M.; Teymourian, H.; Wang, J. Touch-based stressless cortisol sensing. *Adv. Mater.* **2021**, *33*, 2008465.
(54) Kim, K. K.; Kim, M.; Pyun, K.; Kim, J.; Min, J.; Koh, S.; Root, S. E.; Kim, J.; Nguyen, B. N. T.; Nishio, Y.; Han, S.; Choi, J.; Kim, C. Y.; Tok, J. B. H.; Jo, S.; Ko, S. H.; Bao, Z. A substrate-less nanomesh receptor with meta-learning for rapid hand task recognition. *Nat. Electron.* **2022**, *6*, 64−75.
(55) Wei, Y.; Li, X.; Wang, Y.; Hirtz, T.; Guo, Z.; Qiao, Y.; Cui, T.; Tian, H.; Yang, Y.; Ren, T. L. Graphene-Based Multifunctional Textile for Sensing and Actuating. *ACS Nano* **2021**, *15* (11), 17738−17747.
(56) Carey, T.; Arbab, A.; Anzi, L.; Bristow, H.; Hui, F.; Bohm, S.; Wyatt-Moon, G.; Flewitt, A.; Wadsworth, A.; Gasparini, N.; Kim, J. M.; Lanza, M.; McCulloch, I.; Sordan, R.; Torrisi, F. *Adv. Electron. Mater.* **2021**, *7*, 2100112.
(57) de Melo, G. D.; Lazarini, F.; Levallois, S.; Hautefort, C.; Michel, V.; Larrous, F.; Verillaud, B.; Aparicio, C.; Wagner, S.; Gheusi, G.; Kergoat, L.; Kornobis, E.; Donati, F.; Cokelaer, T.; Hervochon, R.; Madec, Y.; Roze, E.; Salmon, D.; Bourhy, H.; Lecuit, M.; Lledo, P. M. COVID-19−related anosmia is associated with viral persistence and inflammation in human olfactory epithelium and brain infection in hamsters. *Sci. Transl. Med.* **2021**, *13*, No. eabf8396.
(58) Ji, Y.; Park, S. M.; Kwon, S.; Leem, J. W.; Nair, V. V.; Tong, Y.; Kim, Y. L. mHealth hyperspectral learning for instantaneous spatiospectral imaging of hemodynamics. *PNAS Nexus* **2023**, *2*, pgad111.

https://doi.org/10.1021/acsnano.3c07283
ACS Nano XXXX, XXX, XXX−XXX